Materials Today Advances 20 (2023) 100441

Contents lists available at ScienceDirect

Materials Today Advances

journal homepage: www.journals.elsevier.com/materials-today-advances/

Solving the puzzle of hierarchical martensitic microstructures in NiTi by (111)-oriented epitaxial films

Klara Lünser [a,b,c,*], Andreas Undisz [d,e], Martin F.-X. Wagner [d], Kornelius Nielsch [b,c], Sebastian Fähler [a]

[a] Helmholtz-Zentrum Dresden-Rossendorf, Institute of Ion Beam Physics and Materials Research, Bautzner Landstr. 400, 01328, Dresden, Germany
[b] TUD Dresden University of Technology, Institute of Materials Science, Helmholtzstr. 7, 01069, Dresden, Germany
[c] Leibniz IFW Dresden, Institute for Metallic Materials, Helmholtzstr. 20, 01069, Dresden, Germany
[d] TU Chemnitz, Institute of Materials Science and Engineering, Erfenschlager Str. 73, 09125, Chemnitz, Germany
[e] Friedrich-Schiller-Universität Jena, Otto Schott Institute of Materials Research, Loebdergraben 32, 07743, Jena, Germany

ARTICLE INFO

Keywords:
NiTi
Martensitic microstructure
Epitaxial films
Shape memory materials

ABSTRACT

The martensitic microstructure decides on the functional properties of shape memory alloys. However, for the most commonly used alloy, NiTi, it is still unclear how its microstructure is built up because the analysis is hampered by grain boundaries of polycrystalline samples. Here, we eliminate grain boundaries by using epitaxially grown films in $(111)_{B2}$ orientation. By combining scale-bridging microscopy with integral inverse pole figures, we solve the puzzle of the hierarchical martensitic microstructure. We identify two martensite clusters as building blocks and three kinds of twin boundaries. Nesting them at different length scales explains why habit plane variants with $\langle 011 \rangle_{B19'}$ twin boundaries and {942} habit planes are dominant; but also some incompatible interfaces occur. Though the observed hierarchical microstructure agrees with the phenomenological theory of martensite, the transformation path decides which microstructure forms. The combination of local and global measurements with theory allows solving the scale bridging 3D puzzle of the martensitic microstructure in NiTi exemplarily for epitaxial films.

Author contributions

K.L. and S.F. conceived and interpreted the experiments together with M.W. K.L. prepared the sample, and performed SEM and XRD experiments and calculations under the supervision of K.N. and S.F. A.U. carried out the TEM experiments. K.L. and S.F. wrote the manuscript with contributions and discussions from all authors.

1. Introduction

NiTi is the most commonly used shape memory material that is applied in medical technology, aerospace and for elastocaloric cooling [1–4]. In form of thin films, NiTi is of particular interest for microactuators [5,6], elastocaloric microcoolers [7] and neurosurgery [8]. All these applications are based on a martensitic transformation, a reversible transformation between the high temperature austenite phase and the low temperature martensite phase that can be induced by temperature and stress. As the shape memory properties are controlled by the martensitic transformation and the resulting martensitic microstructure, lots of work has been dedicated to understanding the formation of this microstructure. To predict and improve properties, an exact model of the microstructure and how it forms is needed. Unfortunately, the self-accommodated martensitic microstructure in NiTi still is a complex puzzle with several unanswered questions and various contradicting observations, which are summarized in detail in section 2, focusing on martensite obtained by stress-free cooling. Specifically, the 3-dimensional assembly and hierarchy of the martensitic microstructure are unclear. Moreover, while theories exist that predict the microstructure, their predictions often do not match experimental results. Although twin boundaries are the most obvious feature of martensite at all length scales, it is not clear why some occur more often than others.

Two factors make these open questions especially difficult to answer: First, the martensitic microstructure is strongly influenced by defects and thus varies depending on precipitates, dislocation density and grain

* Corresponding author. Helmholtz-Zentrum Dresden-Rossendorf, Institute of Ion Beam Physics and Materials Research, Bautzner Landstraße 400, 01328 Dresden, Germany.
E-mail address: k.luenser@hzdr.de (K. Lünser).

https://doi.org/10.1016/j.mtadv.2023.100441
Received 11 August 2023; Received in revised form 28 October 2023; Accepted 5 November 2023
Available online 18 November 2023

boundaries [9–14]. Especially grain boundaries can influence the microstructure in an unpredictable way. Second, most measurement techniques only probe a very small sample fraction and usually just one particular length scale of the martensitic microstructure: Transmission and scanning electron microscopy (TEM and SEM) can measure the orientation of interface boundaries, the orientation relation between variants, the shape of nuclei and clusters [15–19], but cover only a marginal volume of the sample. Microscopy can easily miss features smaller and larger than applied magnification range, and usually misses features below the surface. Though X-ray techniques provide information on the integral variant orientation on a statistically sound basis, in most cases they do so without sufficient spatial resolution [20]. New 3D XRD combines both, but the resolution does not yet resolve the intricate features of thermally induced martensite [21]. This means that the martensitic microstructure is rarely comprehensively analyzed across all length scales – from atomic to macroscopic scale – at the same time.

Here, we solve the puzzle of the martensitic microstructure in epitaxial NiTi films using a comprehensive approach. Epitaxial films are the thin film equivalent of a single crystal in bulk, but additionally have a defined orientation with respect to the substrate used for growth. Through the interface with the substrate, the films are constrained on one side. They can be prepared with several techniques and on different substrates [22–25]. Epitaxial films offer several advantages for the analysis of the martensitic microstructure: First, the defined orientation relation allows for a straightforward analysis of twin boundary and habit plane orientations. Second, the films do not contain large-angle grain boundaries and therefore eliminate the unclear influence of grain boundaries on nucleation and growth of martensite. Third, epitaxial films offer the unique possibility for a comprehensive analysis by combining the results of several experimental techniques for the same film. For a scale-bridging microstructural analysis, we use scanning and transmission electron microscopy to understand the martensite clusters and interfaces from the nm up to μm length scale. As a complementary method, we apply X-ray techniques, which probe several mm of material and therefore provide a statistical overview of the variant orientation. A similar approach has already been used for the Ni–Mn-Ga system, which exhibits a different crystallography [26]. Here, we examine a second system to probe if the hierarchically nested microstructure across all length scales is a general feature of martensite in shape memory alloys.

In this paper, we first give an overview on the martensitic puzzle in NiTi– many pieces of experimental observations and theoretical concepts, which do not yet fit together. To further understand this puzzle, we analyze the microstructure of epitaxial NiTi films by local microscopy and assemble the different pieces of the hierarchical microstructure step-by-step from the smallest to the largest length scale. We show that the smallest building block of the martensitic microstructure consists of two habit plane variants and that this cluster grows and branches out to form larger clusters. Then we confirm and extend these results using integral measurements gathered from X-ray techniques and we finally compare our results to bulk NiTi.

2. The martensitic puzzle in NiTi

This section introduces the most important concepts, definitions and nomenclature of martensitic transformations and microstructures as well as martensite theories and it illustrates why the complexity of the martensitic microstructure has left lots of questions unanswered.

At the length scale of the unit cell, the martensitic transformation involves a symmetry reduction from the cubic B2 austenite to the monoclinic B19' martensite, resulting in 12 energetically equivalent martensitic variants. Transforming austenite to martensite proceeds through nucleation and growth and therefore requires compatible phase boundaries between the austenite and the martensite (habit planes) and compatible boundaries between different martensitic variants (twin boundaries). The combination of two variants with a twin boundary, which together have a habit plane to the austenite, is called habit plane variant (HPV). Often, one variant occurs with a higher ratio compared to the other, which are accordingly named majority and minority variants. Twin boundaries and habit planes can only form on very specific planes, which depend on the crystal structure and lattice parameters of austenite and martensite. Moreover, the combination of multiple variants can reduce the elastic strain energy of a nucleus by self-accommodation [27]. Additionally, stress has strongly influences which kind of variants, twin boundaries and thus martensite clusters form, and both types of stress must be considered: external and created by defects [12,28,29]. The geometry of nucleating martensite clusters is thus governed by several boundary conditions, leading to a very complex martensitic microstructure [30] – a three-dimensional martensite puzzle.

The phenomenological theory of martensite crystallography (PTMC) can be used to understand and predict the martensitic microstructure in NiTi. This continuum theory is based on Wechsler, Lieberman and Read [31] as well as Bowles and Mackenzie [32] and is used here as described by Bhattacharya [33]. As input parameters, the lattice parameters of austenite and martensite and the lattice correspondence between both phases is used. For every pair of two different martensitic variants, it is checked whether a compatible twin boundary can be formed. If a twin boundary is possible, a specific ratio of both variants might be able to form a compatible habit plane to the austenite. The PTMC allows for calculation of the orientation and type of twin boundary, the orientation of the habit plane, the variant ratio, and the orientation of both variants with respect to the austenite.

For NiTi, the PTMC predicts eight different twin boundaries, however, only four of them can also form habit planes [30]. Not all predicted twin boundaries and habit planes have been observed experimentally. The most commonly observed twin boundary in bulk NiTi, which is also predicted by the PTMC, is the $\langle 011\rangle_{B19'}$ Type II twin boundary [34–36]. For the HPVs with these $\langle 011\rangle_{B19'}$ Type II twin boundaries and $\{942\}_{B2}$ habit planes, Miyazaki et al. [15] introduced a naming system, which we will also use in this paper. The twelve possible individual variants are called 1–6 and 1'-6', depending on their orientation relation to the austenite. The 24 possible HPVs are then called 1(+)-6(+), 1(−)-6(−), 1'(+)-6'(+) and 1'(−)-6'(−) (see e.g. tab. 3 in Ref. [16]). Each HPV has its specific habit plane, while one specific twin boundary is shared by two HPVs.

Although the PTMC is widely established, the theory does not answer all questions, e.g. because it fails to predict why certain twin boundaries occur as opposed to others [19]. Moreover, the complexity of the martensitic microstructure becomes apparent when looking at the research, which has not been able to work through some inconsistencies. Regarding twin boundaries, $\langle 011\rangle_{B19'}$ Type II, $\{11\bar{1}\}_{B19'}$ Type I, $\{011\}_{B19'}$ Type I, $(100)_{B19'}$ compound and $(001)_{B19'}$ compound twins have been reported, sometimes in the same sample [34–38]. Although it is mostly agreed that $(001)_{B19'}$ compound twin boundaries are dominant in nanocrystalline NiTi [29] and $\langle 011\rangle_{B19'}$ Type II twin boundaries are the most prominent in larger grained and single crystalline material [30], predicting the type of twin boundaries in a sample remains difficult. Also, the orientation of habit planes was found to be roughly $\{942\}_{B2}$, however, measurements of the orientation show lots of scatter [30]. The self-accommodated microstructure has been examined as well – with partly contradicting results reported in the past: Miyazaki et al. [15] analyzed the microstructure in single-crystalline NiTi and found a triangular self-accommodation with three of four HPVs clustered around $\{001\}_{B2}$. In contrast, Madangopal et al. [39] reported a triangular morphology around the $\langle 011\rangle_{B2}$ trace. Nishida et al. [16] extended these results by examining NiTi polycrystals in {111}-oriented grains and found minimum units of two HPVs also around the $\langle 011\rangle_{B2}$ trace. By adding more HPVs to these units, triangular, rhombic and hexagonal shapes with three, four and six clusters can be created [16]. In addition, they described the characteristics of all occurring interfaces [40] and confirmed the results with theoretic calculations [41]. Although this

paper series [16,40,41] elucidates the most prominent clusters in bulk NiTi, it is still unclear how these clusters are grouped together to form the entire martensitic microstructure. With all those inconsistencies in mind, the martensitic microstructure in NiTi still remains puzzling.

3. Methods

To obtain a single-crystalline austenitic state for our experiments, an epitaxial NiTi film in (111)-orientation was deposited at elevated temperatures. During cooling from the deposition temperature to ambient, the austenite transformed into martensite, creating differently oriented twinned martensitic variants. As with bulk single crystals, the epitaxially grown films are not anymore single-crystalline within the martensitic state in a strict sense. As described in detail before [42], the epitaxial NiTi film was grown with DC Magnetron Sputter deposition to a thickness of 1000 nm on an $Al_2O_3(0001)$ substrate by Crystec GmbH. Between the film and the substrate, a 50 nm thick Cr buffer was deposited at a substrate temperature of 500 °C, whereas the film was deposited at 525 °C. The film was examined as deposited, without any additional heat treatment or cycling. The analyzed martensitic microstructure was therefore obtained by cooling the crystalline film from deposition temperature. The film is Ti-rich with a Ni-content of 47.2 at% Ni. SEM micrographs were taken with a LEO 1530 Gemini microscope by Zeiss, either with a voltage of 20 kV with a Backscatter electron detector or with a voltage of 2.5 kV using an Inlens detector. For in-situ SEM (supplementary Movie M1), a heating stage by Kammrath & Weiss GmbH was used. For the movie, the image shift was corrected with a MATLAB script for spatial drift correction [43]. For transmission electron microscopy (TEM), a lamella was cut from the film using Focused Ion Beams (FIB) with a FEI Helios NanoLab 600i. A NEOARM 200F by JEOL was used for the TEM measurements with an acceleration voltage of 200 kV. Some images were taken in scanning TEM (STEM) mode using a bright-field detector. Pole figures were measured with a PANalytical X'Pert with Cu K_α radiation. Inverse pole figures were calculated with the MTEX software package [44,45]. For the calculation of inverse pole figures, the following pole figures were used: $(002)_{B19'}$+ $(101)_{B19'}$, $(022)_{B19'}$+$(121)_{B19'}$, $(111)_{B19'}$+$(012)_{B19'}$ and $(\bar{1}11)_{B19'}$. Due to the similarity of lattice plane distances of some lattice planes, several lattice planes were captured in one pole figure. For the inverse pole figures, this required a separation of the measured pole figure data. Details about this separation can be found in the supplementary information.

For the calculation of martensitic variants, habit planes and twin boundaries, we implemented the PTMC in a MATLAB code [46], which was adapted and enhanced from Ref. [26]. We use the habit plane and twin plane orientation to compare with the traces of those boundaries in microscopy images. Additionally, we use the rotations of the variants to calculate the orientation of martensitic variants for comparisons in pole figures and inverse pole figures. For inverse pole figures, we calculate the reciprocal lattice vector of the martensitic variants that points into a certain sample direction and pass this vector to MTEX for plotting [44,45].

For our calculations, we used the lattice parameters of $a_0 = 0.3015$ nm for the austenite and $a_M = 0.2885$ nm, $b_M = 0.4120$ nm, $c_M = 0.4622$ nm and $\beta = 96.8°$ for the martensite [47]. Although the film is analyzed in martensitic state, we use B2 coordinates to give the orientation of twin boundaries and habit planes. Using B2 is possible in our case, as our film is grown epitaxially within the austenite state. Thus, we always know the orientation of austenite – in contrast to polycrystalline bulk. This helps for a more intuitive understanding, as every martensitic variant has its own coordinate system, which would complicate any comparison. For better readability, the orientations of twin boundaries and habit planes are rounded to integers. This gives $\{034\}_{B2}$ planes for the Type II $\langle 011\rangle_{B19'}$ twin boundaries (the twinning plane in martensite coordinates is roughly $\{334\}_{B19'}$). For habit planes, the exact values of $\{0.89\ 0.4\ 0.22\}_{B2}$ are rounded to $\{942\}_{B2}$.

4. Results

4.1. Overview of the hierarchical microstructure

To understand the formation of the martensitic microstructure in NiTi, we investigate an epitaxial film in (111)-orientation in real and reciprocal space. At each length scale, we identify characteristic clusters, consisting of twin boundaries and phase boundaries. Before analyzing each cluster in detail, it is helpful to obtain an overview of the hierarchy and the different types of clusters nested into each other. In Fig. 1, the top row of the figure shows SEM micrographs with a decreasing magnification level from (a) to (c). In the bottom row, the cluster observed on a specific length scale is sketched. Each larger length scale is constructed of building blocks that were introduced on the length scale before: On the microscale, a "V-cluster" is present, which obtained its name due to its shape. On the mesoscale, a larger, "triangle cluster" becomes visible, which has a V-cluster at its tip and contains many more inside. On the macroscale, the triangle clusters can exist in three different orientations that make up most of the visible martensitic microstructure. Throughout all clusters and length scales, three kinds of twin boundaries occur: microscopic, mesoscopic and macroscopic twin boundaries, which are also sketched in Fig. 1. In the following, we will use the term "twin boundary" for all boundaries between variants exhibiting a symmetry relation. To distinguish the different length scales within the hierarchical twin-within-twins microstructure, we will add their characteristic length scale. Variants connected by microscopic and mesoscopic twin boundaries exhibit a mirror or rotation symmetry and are thus type I, II or compound twin boundaries, as known from textbooks [33]. In contrast to this, macroscopic twin boundaries occur at a much larger length scale and connect variants with the 3-folded rotation symmetry of austenite. Though macroscopic twin boundaries are thus no twin boundaries in the strict textbook sense, we use this term, as it is helpful for a scale bridging description of the hierarchical microstructure. Indeed, a similar hierarchy was also observed in martensitic material exhibiting a different crystal symmetry like Ni-Mn-Ga [26,48].

In the following sections, we analyze the microstructural features on each length scale, starting from the microscale. At each scale, we first present the experimental results from microscopy measurements. From these microscopy images, we identify interface boundaries such as twin boundaries and habit planes. The knowledge of the boundary orientation allows us the construct a 3-dimensional model of the martensite cluster and to propose a model for its growth. Then, we describe how the clusters are interconnected and span all three length scales, creating the hierarchical martensitic microstructure.

4.2. Microscale

We start the detailed description on the microscale, as the smallest building block presented here influences features on all larger length scales. An example of this building block, which we call V-cluster, is shown in detail in Fig. 2. This figure gives a comprehensive overview of various details of the cluster. We now explain step by step how we derive its 3D geometry, sketched on the top right. In an SEM image (Fig. 2(a), top view) and TEM image (Fig. 2(c), cross section), the cluster and its interfaces are visible in two different perspectives. To identify the boundaries, we go through the following steps: First, we measure the traces of the boundaries in both images, which is straight forward as we know the orientation of the NiTi austenite due to its epitaxial growth. Next, we separate twin boundaries from outer interfaces of the cluster: We attribute interfaces inside of the V-cluster to traces of twin boundaries (marked with dashed lines in all figures), while the interfaces on the outside are traces of former habit planes (marked with dash-dotted lines). These interfaces originally connected the martensitic cluster to the surrounding austenite, until this austenite transformed to martensite as well. Knowing two traces of these interface planes allows for a unique determination of their orientation. Afterwards, we compare these planes

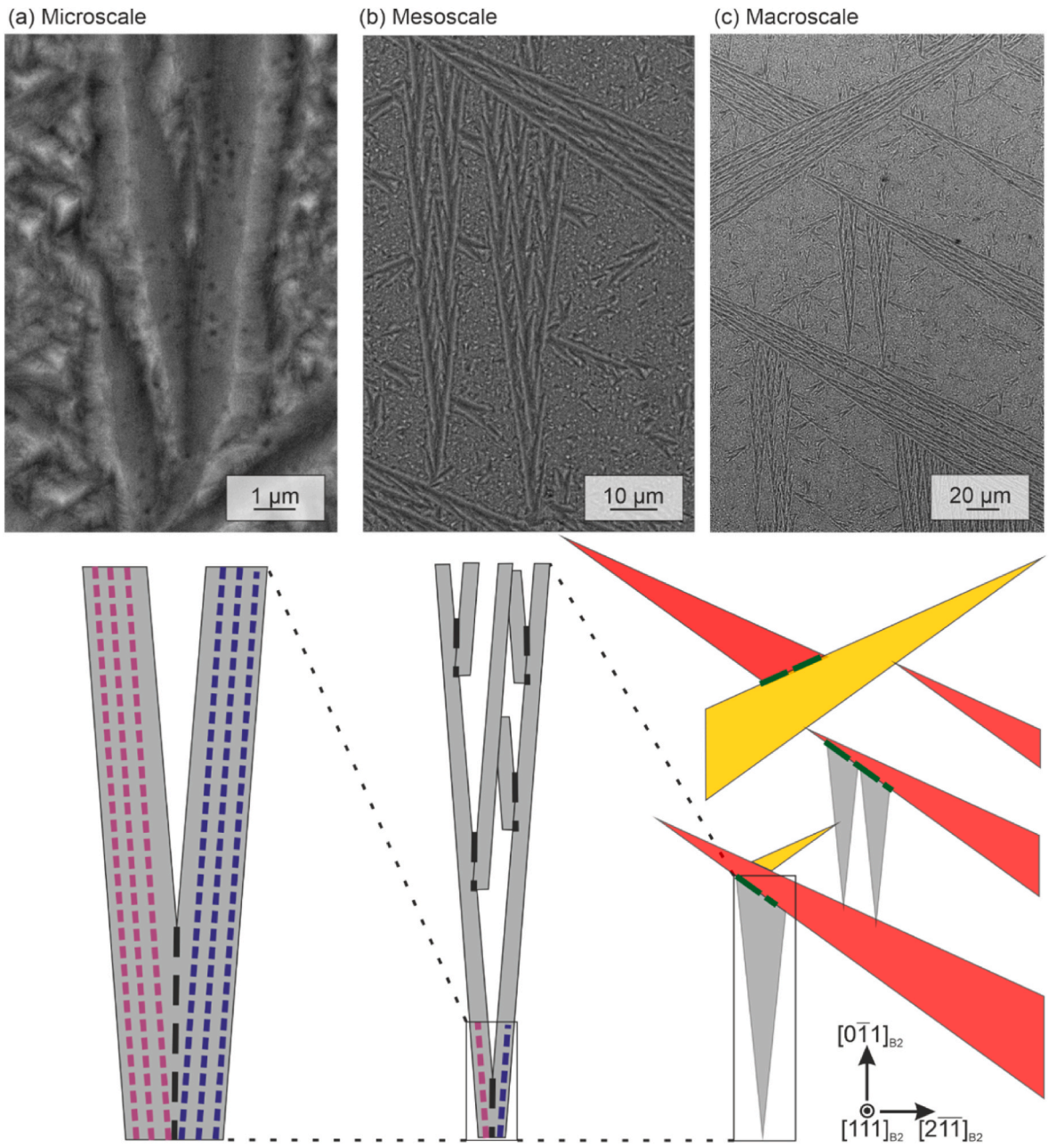

Fig. 1. Overview of the hierarchical martensitic microstructure in (111)-oriented epitaxial NiTi film from micro- to macroscale. The microstructure consists of characteristic twin boundaries and features on different length scales that are nested into each other. The top row shows SEM images in which these features are visible, the bottom row sketches the characteristic twin-boundaries and clusters. (a) On the microscale, the microstructure consists of $\langle 011\rangle_{B19'}$ Type II twin boundaries (microscopic twin boundaries, purple and pink dashed lines) that are parallel to each other inside of an HPV. Two HPVs are connected to form a V-shaped cluster. The connection is formed by a $\{11\bar{1}\}_{B19'}$ Type I twin boundary (mesoscopic twin boundary, black dashed line). (b) When the V-Clusters grow, they can grow into larger triangle clusters. For this, additional $\{11\bar{1}\}_{B19'}$ twin boundaries are introduced. (c) Because of the three-fold symmetry of the (111)-oriented austenite, the V-Clusters and triangles can grow in three equivalent directions. This leads to a third type of twin boundaries, the macroscopic twin boundaries (green dashed lines). These boundaries form where triangles of different orientations grow together.

to the planes predicted by the PTMC (see method section for details about this calculation).

For the V-cluster, this procedure gives a set of four equivalent twin boundaries: $(034)_{B2}$, $(043)_{B2}$, $(0\bar{3}4)_{B2}$ and $(0\bar{4}3)_{B2}$, which are $\langle 011\rangle_{B19'}$ twin boundaries using the B19′ unit cell. The habit planes are $(429)_{B2}$, $(4\bar{2}9)_{B2}$, $(\bar{4}92)_{B2}$ and $(\bar{4}\bar{9}2)_{B2}$. All traces are also sketched in Fig. 2(b) and (d). For a stereographic projection of the involved twin boundaries, see Supplementary Fig. S2. These planes are known from both, the PTMC and experiments of bulk NiTi [16,30,49]. Following the convention of Miyazaki et al. [15], this corresponds to the presence of the HPVs 3'(−), 5(−), 6(−) and 3(+). In addition to the trace analysis, we performed TEM diffraction to confirm the twin relationship between the variants (Fig. 2(g) and (h)). The $\langle 011\rangle_{B19'}$ twin boundaries are Type II twin boundaries, which means that their twinning plane is irrational. This explains why the twin boundaries are several atomic layers thick and do not appear atomically sharp in high resolution TEM (HRTEM) images (Fig. 2(f)). These twin boundaries occur on a small length scale with a spacing of roughly 10–20 nm. To differentiate them from other twin boundaries in the hierarchical microstructure, we call them *microscopic twin boundaries*. The measured orientation of the twin boundaries fits

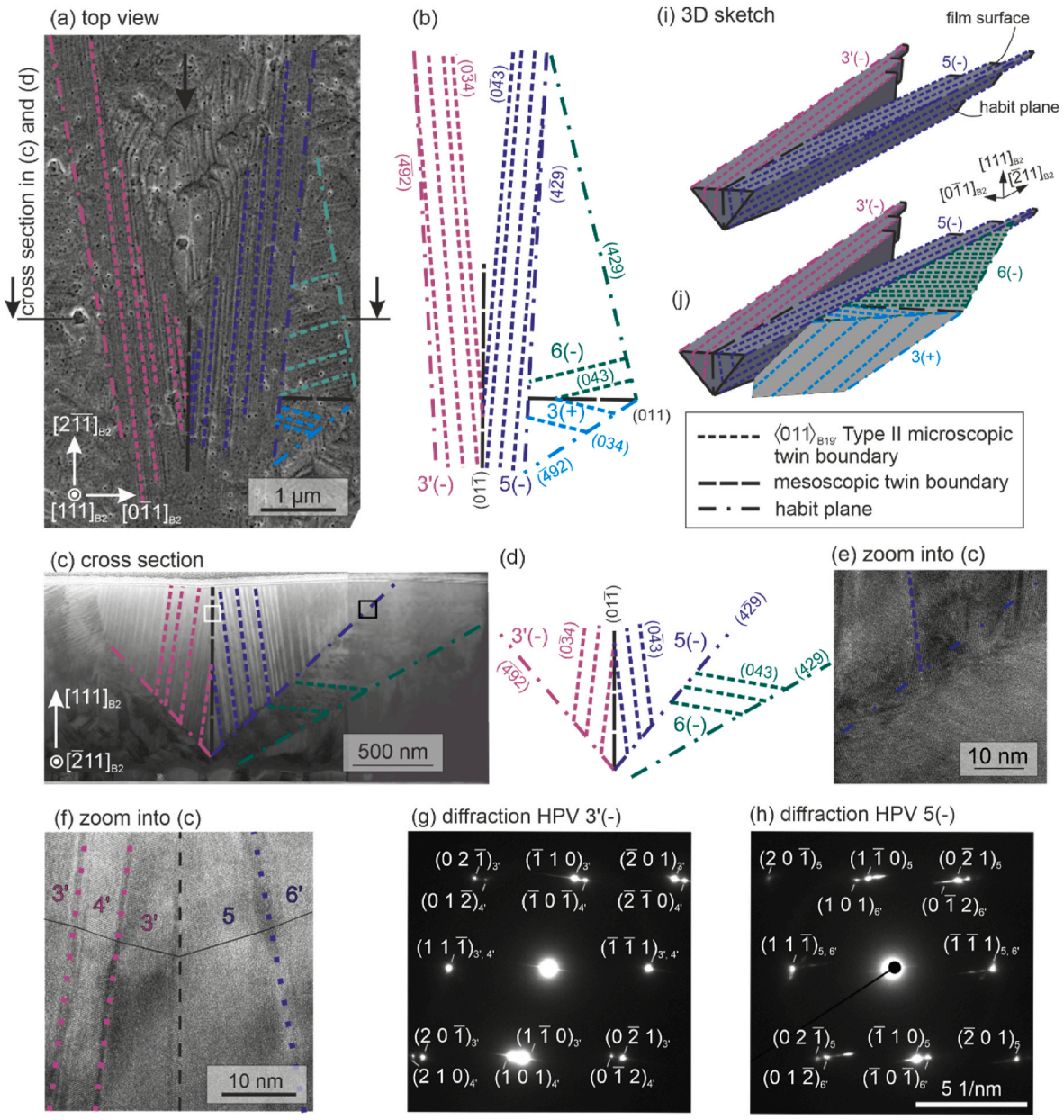

Fig. 2. Deriving the 3D geometry of a V-cluster, sketched in the top right. (a) SEM micrograph showing the top view of a V-cluster, where its V-shape becomes apparent. Microscopic twin boundaries (dashed lines), mesoscopic twin boundaries (dashed lines) and habit planes (dash-dotted lines) are marked. (b) Sketch of twin boundary and habit plane traces with the corresponding HPVs and plane orientations. All planes belonging to one HPV are marked with the same color. The V-cluster contains several HPVs: 3′(−) in pink and 5(−) in purple make up the main part, and 3(+) in blue and 6(−) in green the side part of the cluster. All HPVs have $\langle 011\rangle_{B19'}$ Type II twin boundaries, which are labelled in austenite coordinates with $\{034\}_{B2}$. The habit planes are from the $\{942\}_{B2}$ family. The HPVs 3′(−) and 5(−) as well as 3(+) and 6(−) are connected to each other with a mesoscopic twin boundary. These twin boundaries serve as mirror planes between the respective HPVs and are $\{011\}_{B2} = (11\bar{1})_{B19'}$ Type I twin boundaries. (c) STEM image showing a cross section of the V-cluster. Interface boundaries are marked in accordance with (a). (d) traces of twin boundaries and habit planes in cross section. (e) HRTEM micrograph of the habit plane. The area in which this image was taken is marked with a black square in (c). (f) HRTEM micrograph of the microscopic and mesoscopic twin boundaries (white square in (c)). The microscopic Type II twin boundaries have a thickness of several atomic layers, in contrast, the mesoscopic Type I twin boundary is nearly atomically sharp. The solid line marks the orientation of atom columns as a guide to the eye and visualizes the twin relationship between the variants. (g) and (h) electron diffraction patterns taken from HPVs 3′(−) and 5(−), respectively (see Supplementary Fig. S1 for exact positions). Both patterns contain reflexes from majority variants (3′ and 5) and minority variants (4′ and 6). The mirror symmetry between the patterns coming from the mesoscopic twin boundary can be seen as well. (i) Schematic drawing of the V-Cluster in 3d perspective involving only the "main part" (HPVs 3′(−) and 5(−)). In (j), the "side part" (3(+) and 6(−)) is included as well.

very well to the prediction from PTMC: In the SEM image, the angle of the twin boundary in relation to the black dashed line is 5.3° in the top view and 7.9° in the cross section, which differs only marginally from the calculated values of 5.4° and 7.6°. Interestingly, the habit plane exhibits a larger deviation from the calculation: the measured values are 8° in the top view and 47° in the cross section – a deviation of roughly 5° from the calculated values of 3.9° and 51.5°. We will address the origin of this difference in the discussion section.

As the V-cluster is constructed from different HPVs, we now examine the interfaces between the different HPVs. We start with the boundary between the two HPVs 3′(−) and 5(−), which is marked with a black, dashed line. In both, top view and cross section, these HPVs are in mirror

symmetry to each other. The orientation of the mirror plane can again be inferred from its traces to be $(01\bar{1})_{B2} \approx (11\bar{1})_{B19'}$. The mirror symmetry between HPVs 3′(−) and 5(−) is also visible in the diffraction patterns (Fig. 2(g) and (h)). This mirror plane was predicted as a suitable interface between 3'(−) and 5(−) due to its kinematic compatibility [41], and it is known from bulk NiTi [34], where it has been called junction plane [16]. Here, we will call it *mesoscopic twin boundary*, as this illustrates the hierarchical nesting of the different twin boundaries. The mesoscopic twin boundaries occur on a larger length scale compared to the microscopic twin boundaries; in the film shown here they are spaced roughly 2 μm–5 μm apart. Mesoscopic twin boundaries already bridge the transition to the mesoscale, where these twin boundaries also play an important role.

Up to now, all described boundaries and habit planes are known from NiTi bulk, demonstrating that epitaxial films provide an interesting comparison for the analysis of the martensitic microstructure also in bulk NiTi. As our study covers all length scales, we can also observe new features, which occur quite often. Adjacent to most sides of the V-clusters, we observe a peculiar microstructure, which we call "side part". In Fig. 2, the side part consists of the 3(+) and 6(−) HPVs, which are connected by the same type of $(011)_{B2} \approx (11\bar{1})_{B19'}$ mesoscopic twin boundary connecting both sides of the V-cluster. The side part can also grow on the other side of the V-cluster, involving an equivalent set of HPVs. Indeed, in the whole film, the number of V-clusters with the side part on the right and on the left side is roughly equivalent. Some V-clusters also have both side parts. The side part in Fig. 2 consists of HPVs 6(−) and 3(+), which connect to 5(−) of the V-cluster. Although predictions for possible interfaces between HPV 5(−) and 6(−)/3(+) exist [50], they do not fit to the interface observed here. Since the side part does not occur for all V-clusters, we can attribute the interface between the side part and the main part of the V-cluster to the original habit plane of HPV 5(−). Within the discussion section, we will describe how and why a habit plane becomes an interface boundary between different variants and consequences of this process for the orientation of habit planes. For this discussion, details of this boundary are helpful, which can be identified in the HRTEM image (Fig. 2(e)). The boundary is several nm wide and appears to be disturbed, without any clear twin relation between the involved variants. Incompatible and broad interfaces between HPVs are not uncommon in NiTi [40], indicating that the energy required to form such an interface is relatively low.

To conclude, our approach of analyzing traces enables to identify all interfaces occurring within and around the V-cluster. By combining the top view and the cross section, and using the habit plane and twin boundary orientation, we can construct a 3D model of the V-cluster. This model is shown in Fig. 2(i) for the main part of the V-cluster and in Fig. 2 (j) including the side part. The cluster is mostly enclosed with habit planes on the sides. However, this 3D view allows to identify small areas at the tip and at the ends of both arms, which are neither twin boundaries nor habit planes. With this, the V-cluster is partly encapsulated by incompatible planes, which play an important role during the cluster's growth, as described in the next section.

4.3. Growth scenario of the V-cluster

In this paragraph, we propose a model for nucleation and growth of the V-cluster, and we explain the formation of the incompatible interfaces. For this, we consider the different energies involved in the transformation. Creating a martensitic V-cluster within the austenite requires energy to form all interfaces, which includes microscopic and mesoscopic twin boundaries, as well as the energy for the surrounding habit planes. In the stress-free case, the sum of these energies must be outweighed by the gain of energy due to the volume transformed from austenite to martensite. Therefore, the energy of the twin boundaries and habit planes should be low, which is achieved by a good strain compatibility of these interfaces. Indeed, the mesoscopic twin boundary occurring at the core of the V-cluster has been identified as a favorable interface boundary during initial transformation [51]. Regarding the other interfaces, we first consider the tip of the V-cluster, which is missing in the V-clusters. This is unexpected, since the habit planes at the tip of the V-cluster could extend until the habit planes meet (see Fig. 3(a))). However, the tip appears "cut" at a certain point and is replaced by an additional interface. We propose that this is a result of total interface and volume energies. The interface-to-volume ratio becomes larger closer to the tip, because more habit plane area must be created for less volume. At a certain point, it is no longer energetically favorable for the cluster to create a sharp tip and an incompatible interface is created instead (Fig. 3(b)). We observe that all tips are cut with a width of about 1.4 μm, which indicates that this type of energy minimization is a quite robust process. A similar process occurs at both "arms" of the V-cluster, which are in opposite direction to the tip. In fact, a similar argument may well apply to the volume of stress-induced martensite below indents in NiTi bulk samples [52–54]. Once the V-cluster is nucleated, we propose the steps depicted in Fig. 3(c)–(f) as a growth model. In the beginning, a small cluster nucleates, consisting of two HPVs connected by a mesoscopic twin boundary (Fig. 3(c)). The clusters seem to nucleate at the surface, which is reasonable as a free surface can deform easily to accommodate strain [48]. In other words, the absence of constraints at a free surface allows to avoid additional interface (energy). The small cluster is enclosed with habit planes on the sides and with incompatible interfaces at the tip and both arms. By moving the habit planes outwards, the nucleus can grow in width and depth, until it reaches the substrate (Fig. 3(d)). Further growth of the habit planes is then inhibited because this would involve creating additional incompatible interfaces with the rigid substrate. Instead, more volume is transformed to martensite by growing the arms of the V-cluster (Fig. 3 (e)). This only moves incompatible boundaries, but it does not increase their area, making this process energetically favorable. We observe a faceting of this interface (Fig. 2), which allows to increase the volume transformed to martensite without substantially altering the area of the incompatible interface. The area between the facets is then filled with additional martensitic variants, which are visible in Fig. 2(a) in the area marked with a black arrow. Indeed, we observed in in-situ experiments that the martensite in between the arms forms after the nucleation of the V-cluster (see Movie M1 in Supplementary information). The twin boundaries in this area are irregular, and we propose that this originates from the inhomogeneous stress fields created by faceting. The occurrence of these irregular variants can stop the further growth of the V-cluster (Fig. 3(f)). In some cases, the facets can grow, which is further discussed in section 4.3.

Some aspects of this scenario can be confirmed experimentally. As the growth is limited by the film thickness, the clusters have a very uniform size that depends on the film thickness. The ratio of V-cluster width to film thickness can be calculated with the PTMC using the cluster geometry, which gives a ratio of 2:1. For a film thickness of 1 μm, we therefore calculate a width w of 2 μm at the broadest point before the arms separate. The measured value is 2.4 ± 0.1 μm, which reasonably fits to the theoretical value. We tried to resolve the intermediate steps with in-situ SEM experiments (see supplementary Movie M1), but the transition happened too fast to document the growth stages. This indicates that the growth from c) to e) proceeds very quickly once the activation energy for the initial nucleation is overcome. To sum up, most of the geometry of a V-cluster is determined by its compatible interfaces. A few features, however, are controlled by the finite film thickness. This determines the size of the V-clusters, which accordingly is quite uniform.

4.4. Mesoscale

In this section, we will analyze the "triangle cluster" visible at the mesoscale (c.f. Fig. 1(b)) and presented in detail in Fig. 4. In many respects, it resembles a larger version of the V-cluster: It has a similar shape, its acute angle of 13° is similar to the angle of 16° between the

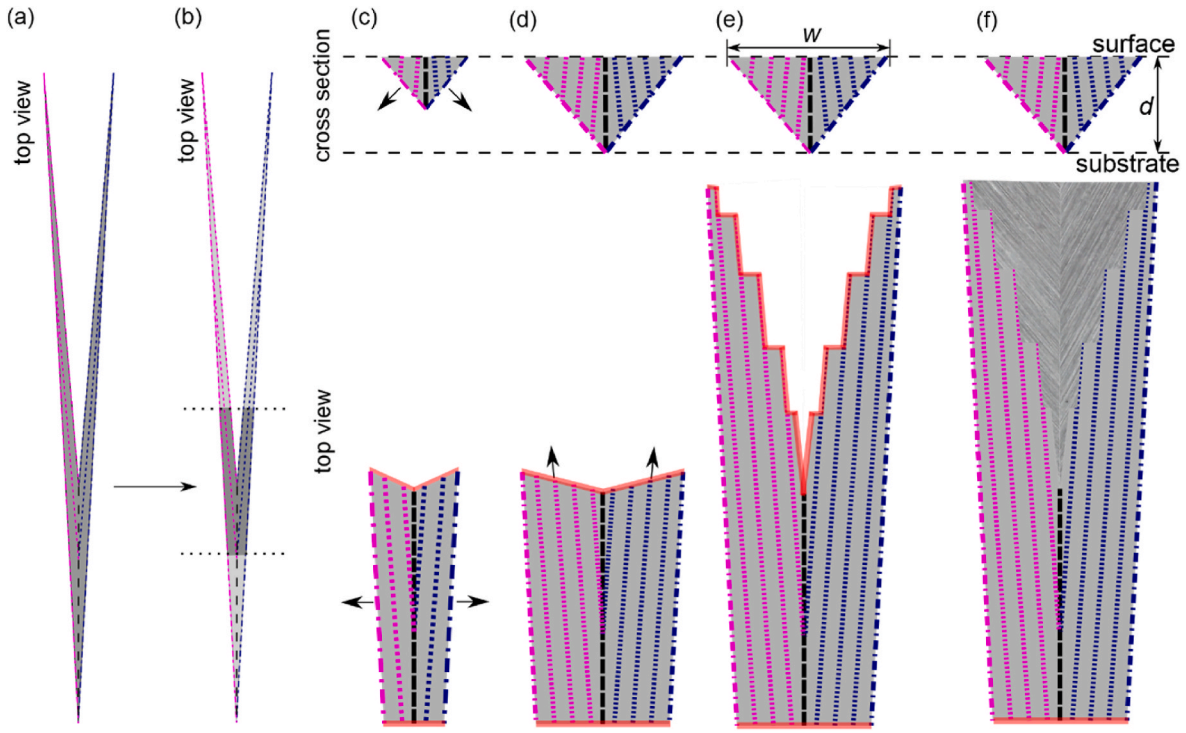

Fig. 3. Growth scenario of the V-cluster. (a) Theoretical shape of V-cluster if habit planes grew until they meet. (b) Observed shape of V-cluster that occurs because the tips of the cluster are cut due to their unfavorable surface-to-volume ratio. (c) Nucleus of the V-cluster in cross-section and top view. The habit planes grow in the direction of the arrows and form intermediate shapes. In (d), the cluster has reached the substrate in depth, meaning that the habit planes cannot grow outwards anymore. The arms of the V-cluster grow in the direction of the arrows, moving the incompatible interface (red). (e) V-cluster with arms that are faceted on the inside. *w* marks the width of the cluster when the tip reaches the substrate. (f) Filling the inner region with irregular martensite (shaded) terminates the growth of the cluster.

habit plane traces of the V-cluster (Fig. 4(a) and (b)) and also the orientations of the twin boundary traces are identical to the V-cluster (Fig. 4(c)). Inside a triangle, we observe needle-like structures that are aligned in parallel to the edges of the triangle (Fig. 4(b)). Because of the similarities, we conclude that the triangle cluster nucleates as a V-cluster and therefore consists of the same HPVs. As a model for the growth from V-cluster to triangle cluster, we propose the scenario shown in Fig. 4(d). Starting point is a V-cluster. The feature that connects the V-cluster and the triangle cluster are the incompatible boundaries at the end of both V-cluster arms. These boundaries are easily movable which makes the arms grow longer with their respective habit planes on the outside (Fig. 4(d) (1)–(3)). The arms grow in length until they meet another cluster or some defect that hinders further growth. This creates the outside boundaries of the triangle cluster. Inside of these boundaries, additional mesoscopic twin boundaries form to branch out more complementary arms (Fig. 4 (d)(5–7)). This creates the needle-like, parallel features observed inside of the triangle cluster. This process continues on both arms of the initial V-cluster until the whole cluster is filled with martensite (Fig. 4(d)(8–9)). When two differently oriented arms meet, they can create the yellow dotted boundary in Fig. 4(b) and (c), which can be identified as an "identity boundary" [26]. This is because the side parts on the opposing sides of the V-cluster share the same variants: 3(+) and 4(+) both consist of the variants 3 and 4 and share the twin boundary $(034)_{B2}$, while 6(−) and 5′(+) consist of variants 5' and 6 with the twin boundary $(043)_{B2}$. This leads to a nearly invisible boundary where both side parts meet.

In consequence, the V-cluster and the triangle cluster consist of the same HPVs and boundaries. Whether a V- or a triangle cluster occurs in the fully transformed microstructure depends on how large the cluster can grow. In case of the V-cluster, the incompatible boundary at the end of the arms transforms to the irregular variants on the inside of the V-cluster. In case of the triangle, the boundary moves outwards to elongate the arms. Therefore, this incompatible boundary connects the micro- and the mesoscale.

4.5. Macroscale

Due to the three-fold inversion symmetry of the austenite in (111)-orientation, the V-cluster can occur in three equivalent orientations, each rotated by 120° around the substrate normal. The V-clusters in equivalent orientations thus consist of other HPVs. The HPVs and mesoscopic twin boundaries are summarized in Table 1.

On the macroscale, the V-clusters and triangles in three different but equivalent orientations exist next to each other. An example of the microstructure on the macroscale is presented in Fig. 5(a). Like in a puzzle, triangles of different sizes are pieced together and form the complete microstructure. The three different orientations are marked in Fig. 5(b) in grey, red and yellow. This suggests the following scenario: during cooling, nucleation starts with very few V-clusters, which transform to triangles. This sparse nucleation leaves large areas untransformed. These areas are filled with smaller triangles. This creates a self-similar, fractal-like microstructure, similar to other materials with martensitic transformations [55,56]. The boundary between the differently oriented clusters introduces a third kind of twin boundary: the macroscopic twin boundary, which is sketched as a green dashed line in Fig. 5(b). In the analyzed film, the distance between the macroscopic twin boundaries spans from 5 to 100 μm. A macroscopic twin boundary is not a twin boundary according to the classical textbooks, as it connects variants only with the 3-folded symmetry of austenite. It is compatible at the macroscopic length scale, as the sample obviously does not fall apart. However, a macroscopic twin boundary is not perfectly strain compatible at the microscopic level, which is evident by its deviation from a

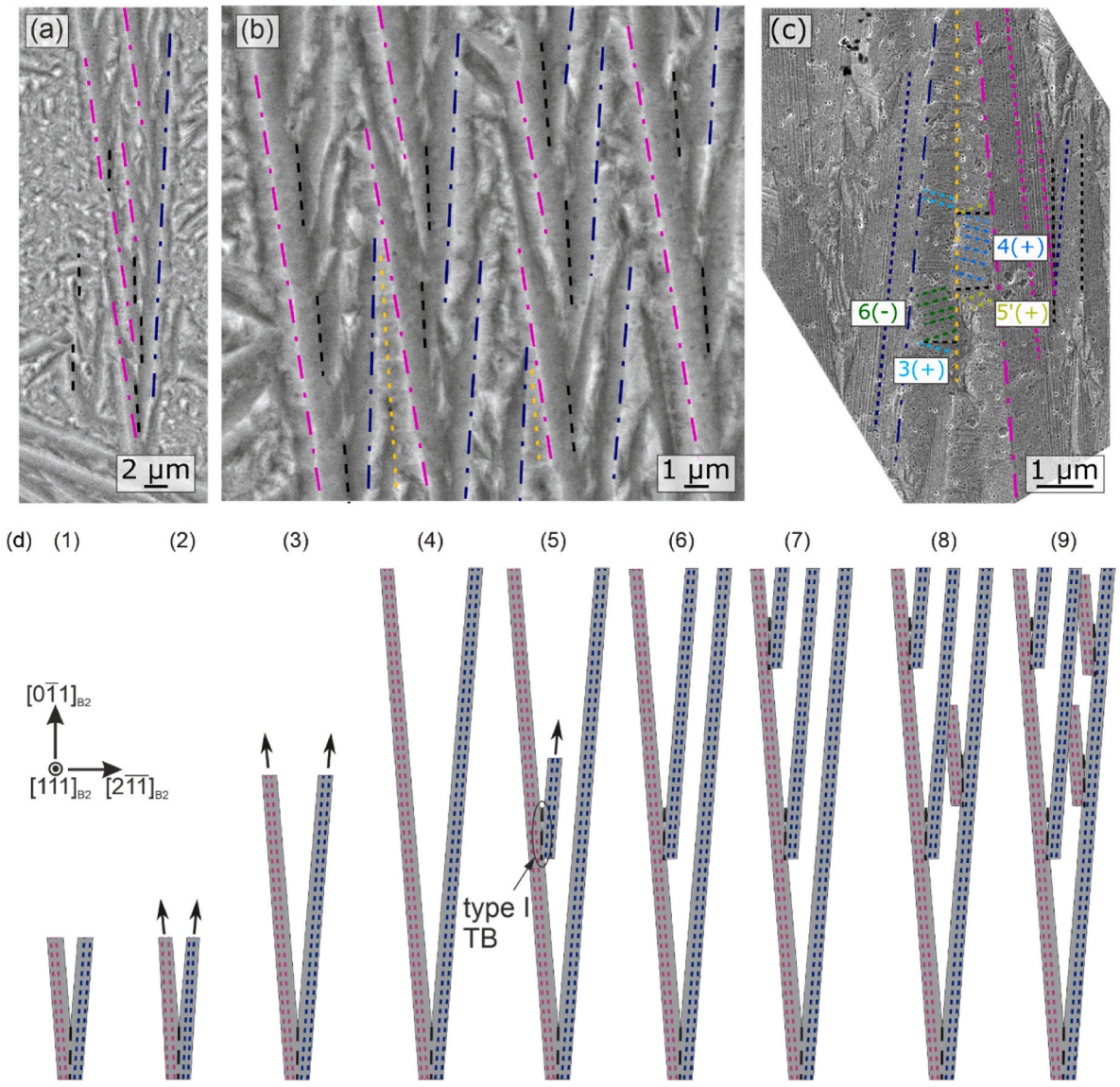

Fig. 4. Detailed view and growth scenario of the triangle cluster on the mesoscale. (a)–(c) SEM micrographs showing the triangle clusters in different magnifications. Habit planes and twin boundaries (TB) are marked following Fig. 2. In (c), two side parts of the V-clusters grow together in a triangle and form an identity boundary (yellow dashed line) (d) Growth scenario: (1–3) growth of V-cluster arms, (5–9) branching inside the V-cluster with additional mesoscopic Type I twin boundaries and growth of new arms. To make the sketch more understandable, the side parts of the V-cluster are not included.

Table 1
HPVs that make up the V-clusters in three equivalent orientations. The mesoscopic twin boundary between the two HPVs in the main V-cluster is given as well. In the present film, some V-clusters have a side part on the left, some on the right and some on both sides.

HPVs in V-cluster main part	Mesoscopic twin boundary	Side part right	Side part left
5(−)/3′(−)	$(01\bar{1})_{B2}$	3(+)/6(−)	5′(+)/4(+)
1(−)/5′(−)	$(\bar{1}10)_{B2}$	5(+)/2(−)	1′(+)/6(+)
3(−)/1′(−)	$(\bar{1}01)_{B2}$	1(+)/4(−)	3′(+)/2(+)

straight plane by faceting and disturbance observed at shorter length scales (Fig. 5(c)). In our opinion the similarities between classical and macroscopic twin boundaries justify using the term twin boundary for all length scales. In conclusion, the microstructure on the macroscale is created by the crystal symmetry of austenite, resulting in three possible orientations of the V-cluster and the triangle cluster.

4.6. Texture of the martensitic film

With microscopy, we were able to identify the prominent martensite clusters in epitaxial NiTi films and explain them on all length scales. Still, TEM micrographs only provide access to a limited volume of the sample and SEM micrographs visualize only the surface of the film. Therefore, it remains unclear if the observed clusters are representative of the entire sample. To make our analysis more complete, we measured the films with X-rays, which scan a large portion of the sample, including

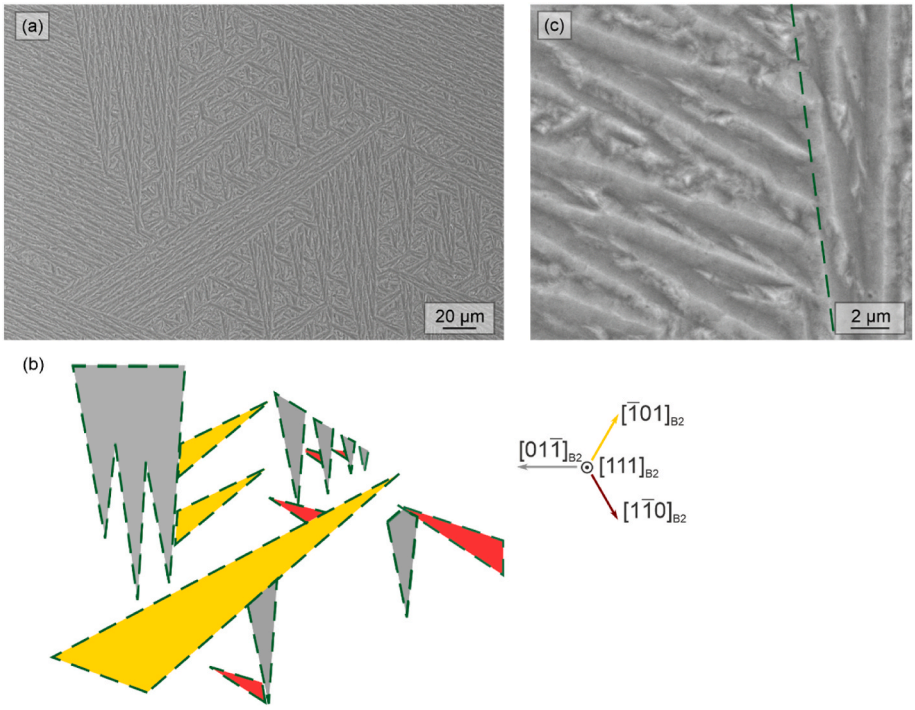

Fig. 5. On the macroscale, macroscopic twin boundaries connect triangles of the three different possible orientations. (a) SEM overview of triangle clusters. They can occur in three different, equivalent orientations due to the symmetry of the (111)-oriented austenite. (b) Sketch of some of the triangle clusters from (a). The different orientations are marked in red, grey and yellow, the macroscopic twin boundary with dashed green lines. The small red triangles between the grey triangles in the upper part of the sketch are an example of the self-similar microstructure. (c) Detailed view of a macroscopic twin boundary where clusters of two different orientations meet. For better visibility, the macroscopic twin boundary is marked with a dashed green line. Due to its origin, the macroscopic twin boundary is only compatible on the macroscale, but neither straight nor regular at the microscale.

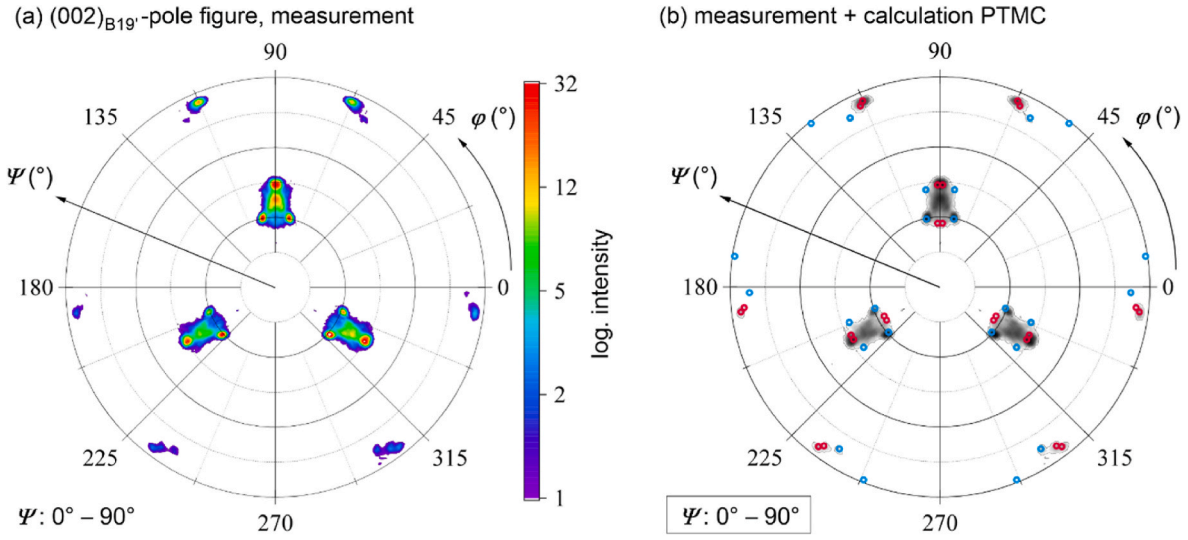

Fig. 6. Comparison of a measured $(002)_{B19'}$ pole figure with martensite theories (a) Measured pole figure ($2\theta = 39.121°$). with logarithmic scale. (b) Comparison of measured pole figure from (a) with poles of the $\{002\}_{B19'}$ planes calculated with PTMC, considering only HPVs with $\langle 011\rangle_{B19'}$ twin boundaries and $\{942\}_{B2}$ habit planes. Each of the 24 HPVs gives two poles in the pole figure, one majority variant marked with red dots and one minority variant marked with blue dots. For better visibility of the theoretical positions, the measured data is shown with a grey scale. Measured high intensity maxima match well with the theoretical positions.

the volume below the surface of the thin film. We measured pole figures to probe the orientation of variants and their frequency and compare the variant orientations with PTMC. This allows to decide which set of HPVs occur and enables us to verify whether the cluster model from the microscopy measurements is valid also on an integral scale.

Fig. 6 shows the $\{002\}_{B19'}$ pole figure of the epitaxial film. The lattice plane distance of $\{002\}_{B19'}$ planes is very close to the distance between $\{101\}_{B19'}$ planes, which is why the measured pole figure exhibits intensity maxima from both lattice planes. To make the figure more intuitive, we separated the $\{002\}_{B19'}$ and $\{101\}_{B19'}$ pole figures (see Supplementary Text and Fig. S4 for details) and only show the $\{002\}_{B19'}$ pole figure here. The pole figure was measured with the substrate parallel to the sample holder, therefore, poles from planes parallel to the substrate appear at $\Psi = 0°$ and poles from planes perpendicular to the

substrate at $\Psi = 90°$. The three-fold symmetry of the (111)-oriented austenite is reflected in the three-fold symmetry of the pole figure. The pole figure exhibits three prominent intensity maxima at $\Psi = \sim 45°$ and six additional maxima close to $\Psi = 90°$, which all correspond to different martensitic variants. For Fig. 6(b), the theoretical positions of intensity maxima of the variants were calculated with PTMC and are superimposed on the measured pole figure. Only HPVs with $\langle 011 \rangle_{B19'}$ twin boundaries and $\{942\}_{B2}$ habit planes were considered because these are dominant in our microscopy measurements. Each of the 24 HPVs gives 2 theoretical positions in the pole figure, one for the majority variant (red dots) and one for the minority variant (blue dots). The comparison shows that areas with high intensity are well explained with the position of majority variants. The lower intensity of the maxima close to $\Psi = 90°$ is due to the measurement setup, where the measured intensity decreases close to $\Psi = 90°$. Also minority variants fit to positions with lower intensity in the measurement. This means that all possible HPVs with $\langle 011 \rangle_{B19'}$ twin boundaries and $\{942\}_{B2}$ habit planes are present in the film. Only few areas with little intensity remain unexplained. At e.g., $\varphi = 90°$ and $\psi = 30–45°$, the intensity in the experiment is smeared over a broader range than predicted by theory, which only gives distinct positions at the outer edges of the observed intensity distribution. Considering that the experimental data is shown on a logarithmic scale, we conclude that PTMC describes the observed orientations well.

Although this pole figure already shows that the PTMC describes the integral microstructure well, one pole figure only gives information about the selected lattice plane. For a comprehensive overview, we measured additional pole figures of different lattice planes as well (see Supplementary Fig. S5). All these pole figures can be combined into inverse pole figures. In contrast to pole figures, which show the orientation of just one lattice plane in all sample directions, an inverse pole figure shows all crystallographic directions pointing into one specific sample orientation. We chose two in plane and the out of plane sample directions for the inverse pole figures depicted in Fig. 7. In addition to well defined maxima, the inverse pole figures exhibit fainter lines connecting these maxima. These artifacts are a well-known phenomenon in inverse pole figures [57]. They arise because the reconstruction of orientation density functions necessary for the calculation of inverse pole figures inherently introduces ambiguity [58]. These so-called ghost lines of low intensity are an artifact of the calculation and do not correspond to actual crystal orientations in the sample. Like for pole figures, the crystal direction of each martensitic variant in the inverse pole figures can be calculated with PTMC. Fig. 7(b) shows these theoretical positions of the crystal directions for the HPVs with $\langle 011 \rangle_{B19'}$ twin boundaries and $\{942\}_{B2}$ habit planes. Here, due to the crystal symmetry, several variants contribute to the same intensity in one inverse pole figure. Like for the pole figures, the positions match the intensity maxima from the measurements well. Minority variants (blue) are less well visible because, in contrast to the pole figures, a linear and not a logarithmic scale is used for the inverse pole figures. To prove that our approach of comparing inverse pole figures with theory works well, we also compared other HPVs calculated with PTMC with our measurement (see Supplementary Fig. S6 and Fig. S7). No other set of HPVs can describe the experiment as well as those shown here.

This observation has two important implications: First, it demonstrates that the model of HPVs and twin boundaries established in the first part of the paper is verified with an additional, independent method. Second, and more generally, this integral method proves that HPVs with $\langle 011 \rangle_{B19'}$ twin boundaries and $\{942\}_{B2}$ habit planes dominate. In contrast to microscopy, the inverse pole figures give statistical evidence that these HPVs make up most of the microstructure.

5. Discussion

5.1. The role of the habit plane after initial cluster formation

By analyzing the V-cluster, we observed that the habit plane of the V-cluster's main part often becomes an intervariant boundary between the main and the side part. In this section, we discuss the role of the habit plane during the transformation and explain the consequences of this conversion. During initial nucleation, a habit plane provides a compatible boundary between the martensitic nucleus and the surrounding austenite. Martensitic nuclei can grow by moving the habit plane outward and thus by transforming more austenite, but this growth is usually stopped once an obstacle is met, e. g. the substrate of a film or a grain boundary in a polycrystalline sample. To increase the volume of martensite further, the habit plane transforms to an intervariant boundary. Already from our postmortem analysis of the V-cluster, we can see that the side part of the V-cluster connects to the main part through a plane with a similar orientation as the original habit plane of the main part. Calculations of the expected interfaces between the

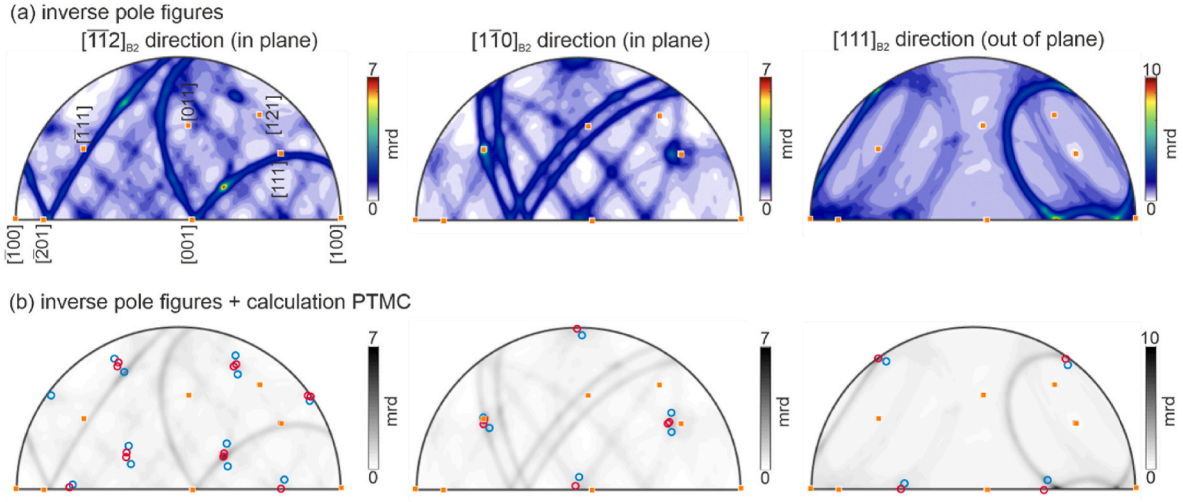

Fig. 7. Comparison of inverse pole figures of the film volume with PTMC. (a) Inverse pole figure calculated from measured pole figures for the three different sample directions. First column: $[112]_{B2}$ direction, second column: $[110]_{B2}$ direction (both in plane), and third column: $[111]_{B2}$ direction (out of plane). Due to the symmetry of the monoclinic martensite, only half of a circle is needed for the representation of all crystal directions. Orange squares mark specific crystal directions, which are annotated in the left inverse pole figure. The results are presented in multiples of random distribution (mrd) units. (b) Comparison of the inverse pole figure with calculated positions according to PTMC, considering only variant combinations with $\langle 011 \rangle_{B19'}$ twin boundaries and $\{942\}_{B2}$ habit planes. Majority variants are indicated with red circles, minority variants with blue circles.

involved HPVs (which worked for the mesoscopic twin boundary) predicted interfaces in $(010)_{B2}$ or $(403)_{B2}$ [41]. Both planes deviate from the observed plane by more than 30°. Indeed, the observed interface seems to be incompatible as it is disturbed and several nanometers wide (see Fig. 2 (e)). To confirm this, we performed in-situ SEM measurements, which show that the side part of the V-cluster nucleates shortly after the main part (see Movie M1 in supplementary Information). Possibly, the habit plane, which is never fully compatible on the atomic scale and therefore contains defects, even serves as a nucleation center for the side part. The short succession of the initial V-cluster nucleation and the nucleation of the side part during cooling supports this hypothesis.

The conversion of the habit plane into an intervariant boundary has two important consequences. First, this means that the formation of martensitic nuclei also influences the formation of the surrounding microstructure. Without knowing that the side part of the V-cluster nucleates after the main part, the interface between both would remain unexplained. In other words, an easily accessible transformation path can result in a microstructure that is not at a global minimum in energy. Second, this observation might explain why determining exact habit planes is so tricky for NiTi. In bulk NiTi, measured values for habit plane orientations exhibit lots of scatter and deviate several degrees from the expected value calculated with PTMC [15,59–61]. Also in our epitaxial films, the habit plane orientations determined from the traces in SEM and TEM measure to $\{742\}_{B2}$ rather than $\{942\}_{B2}$, a deviation of 5°. In all these cases, however, the habit plane orientation was measured post-mortem in samples that were completely transformed to martensite. We suggest that variants with $\{942\}_{B2}$ habit planes form during initial transformation, as our integral X-ray measurements show that the observed variant orientation fits very well to these HPVs. However, during completing the transformation, original habit planes become interfaces between different variants of martensite. Since these interfaces are not fully compatible, the habit plane undergoes some deformation. This deformation depends on the particular variants involved, which then leads to the observed scatter in measurements of the habit plane orientation. PTMC, however, only considers the initial transformation of one nucleus in a defect free, infinite austenite crystal, and thus does not take any further transformation and deformation into account. In our opinion, this is the reason for the differences between calculated and measured habit planes. To prove this hypothesis, we propose to measure the habit plane orientation in-situ and non-destructively during the nucleation stage, for example with X-ray tomography. Due to the small size of the nucleus in epitaxial films, such a measurement is probably more feasible for single-crystalline bulk.

5.2. The complete 3D martensitic microstructure

The observed V- and triangle clusters explain a large portion of the three-dimensional martensitic microstructure. Still, smaller details of this microstructure remain unexplained, for example the areas between the V-clusters (Fig. 1(a), see also Supplementary Fig. S8), and the irregular areas between the arms of the V-cluster (black arrow in Fig. 2 (a)). Clarifying the variants and interfaces in these areas is difficult because these features are too small to resolve in SEM or perfectly cut for TEM. Moreover, the clusters vary strongly, making it hard to identify regular patterns. This irregularity can be explained by considering the transformation pathway as well. In-situ experiments (see Movie M1 in supplementary information) show that, during cooling, the irregular areas transform at lower temperatures than the V- or triangle clusters. Accordingly, in these areas (and the volume below) a higher driving force for transformation is available – and obviously needed. We propose that this is necessary, because the complex geometry of compatible shapes like the V-cluster or other clusters observed in bulk [16] does not allow to fill the remaining irregular volume. The irregular clusters observed in these regions probably need to spend more energy on incompatible interfaces and thus form at lower temperatures. Furthermore, these regions transform next to already existing martensitic clusters. Since self-accommodation is never perfect, the initial martensite clusters create some stress fields in the remaining austenite. Indeed, it was observed [62] that austenite in proximity to a habit plane can even rotate to accommodate the stress created by martensite. This irregular and largely unpredictable stress state of the austenite can influence what martensite variants and clusters occur. Although our local analysis methods leave these intricate and irregular features unexplained, our approach of analyzing epitaxial films captures key and main features. In addition, our (inverse) pole figures show that we can explain nearly all microstructure features in integral measurements, which illustrates that the irregular microstructure forming at the end of the transformation also consists of HPVs with $\langle 011\rangle_{B19'}$ twin boundaries and $\{942\}_{B2}$ habit planes. In simple words, the flexibility of NiTi allows to press the few remaining pieces into the puzzle by brute force.

5.3. Similarities and differences between the martensitic microstructure in NiTi bulk and epitaxial films

In many respects, the martensitic microstructure observed here has many similarities to previous results on bulk NiTi. In particular, we will compare our results to those of Nishida et al. [16] because their bulk samples were (111)-oriented and therefore in the same orientation as our (111)-oriented film. The first similarity is the group of dominant HPVs. In films, we observed HPVs with $\langle 011\rangle_{B19'}$ twin boundaries and $\{942\}_{B2}$ habit planes. These kinds of HPVs have been established as the most dominant HPV in NiTi bulk [60] (at least for single crystals and polycrystals with large grains – results for nanocrystalline NiTi can be quite different [29,63]). Moreover, like for bulk NiTi, the film's martensitic microstructure can be largely explained with PTMC. Not only the microscopic twin boundaries and habit planes, also the mesoscopic twin boundaries are known from bulk NiTi [17,34,40]. This particular mesoscopic twin boundary has a low twin boundary energy and requires little rotation of the variants to form the exact interface [40,51]. This explains why this boundary forms preferentially as an interface between HPVs, both in films and bulk. All these similarities imply that epitaxial films are well suited to study the martensitic microstructure and to examine the influence of a defined constraint.

Local stresses strongly affect martensite variant selection in bulk NiTi [64–66]. Clearly, mechanical constraints, as may be present in epitaxial thin films, are likely to have an impact on the resulting martensitic microstructures. In addition to external stress and stress originating from precipitates, known from bulk, thin films can exhibit a biaxial stress with respect to the thick substrate. As we intended to examine the stress-free state, we avoided stress by epitaxial misfit by using a buffer with minimum misfit [42]. Still, some stress may originate from cooling the film from deposition temperature to ambient due to the difference of thermal expansion coefficients between film and substrate. As quantification of stress in martensitic epitaxial films requires more sophisticated methods [67], we have to leave this aspect for future experiments. We consider this stress to be low, as we neither observed delamination (also not in much thicker films), nor a strong bending of the FIB lamella, which occurs when there is stress between film and substrate. In TEM mode, some bending contrasts became visible but did not exceed what is usually observed for bulk materials. Additionally, the perpendicular view of the interface NiTi/substrate does not indicate towards relief of internal stress.

In some aspects, however, the martensitic microstructure in the epitaxial film differs from bulk. Specifically, the cluster formed from HPVs is different. The most prominent cluster in bulk NiTi was called 6HPVC, a cluster consisting of 6 HPVs arranged in a hexagon-like fashion [16]. The V-cluster was not reported for bulk. In contrast, we did not observe the 6HPVC in our film. Why is the arrangement of the same HPVs different for both types of samples? To answer this question, it is necessary to consider the 3-dimensional constraints acting on the clusters. The substrate of an epitaxial film represents a rigid boundary

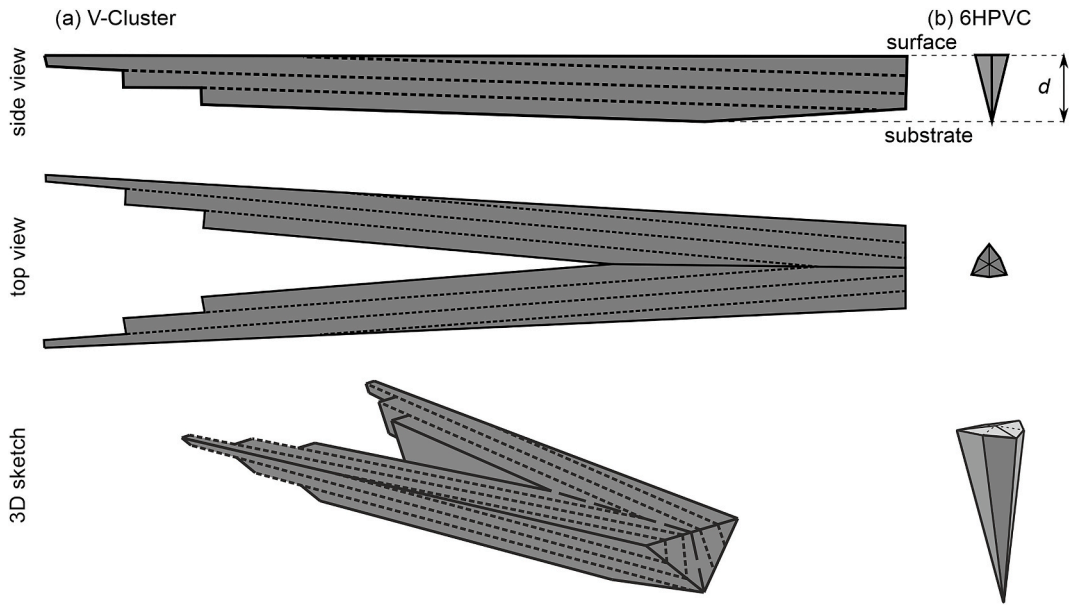

Fig. 8. Comparison of a) V-cluster in (111)-oriented film with the b) 6HPVC known from bulk [16]. Top row: Side view of both clusters, scaled to the film thickness *d*. Middle row: top view of the cluster with the same film thickness. It becomes apparent that the V-cluster can transform more volume than the 6HPVC in the given film geometry. Bottom row: 3D view of the cluster. For better visibility, a different scale is used compared to top and side views.

and confines the transformable volume to a very limited space, in our film to the film thickness of 1 μm. This contrasts with the free surface, which does not represent a constraint and thus favors nucleation. In bulk NiTi, grain size can be up to hundreds of μm, providing plenty of room for clusters to grow. A look at the 3D model of the V-cluster and the 6HPVC in Fig. 8 clarifies why the V-cluster is preferred in films. Both clusters are scaled to the space available in a film, meaning that the depth of the whole cluster cannot be larger than the film thickness. Because of the fixed film orientation and cluster geometry, no rotations of the clusters are possible. It becomes apparent that a 6HPVC cluster only transforms a small volume compared to the V-cluster. Due to the more favorable habit plane-to-volume ratio of the V-cluster, in films they are preferred compared to 6HPVC. Interestingly, the HPVs in the (111)-oriented 6HPVC (2′(+), 2′(−), 4′(+), 4′(−), 6′(+) and 6’(−) [16]) are not present at all in the V-clusters (cf. Table 1). This illustrates how boundary conditions can lead to a variant selection at least for the larger clusters. The integral pole figure measurements show that, in the complete film, all 24 HPVs occur, indicating that the 6 HPVS not occurring within the V-cluster are present in the smaller clusters next to the V-clusters. This example demonstrates that the martensitic microstructure strongly depends on boundary conditions. Compared to bulk materials, where the extension of grains and therefore restrictions by grain boundaries often vary wildly, the substrate in films is a well-defined constraint. This explains the quite regular martensitic microstructure present in the films, which gives us a very high number of identical pieces to solve the NiTi puzzle.

6. Summary and conclusions

Our scale bridging microstructural analysis of epitaxially grown NiTi films combine results from micro- to macroscale to understand the 3-dimensional martensitic microstructure in these films on all length scales. NiTi forms a hierarchical martensitic microstructure, which consists of a nested arrangement of different types of twin boundaries that are all needed to form the complete microstructure: On the smallest length scale, $\langle 011\rangle_{B19'}$ twin boundaries connect two variants of martensite. On the mesoscale, two habit plane variants (HPVs) are joined with a mesoscopic $\{11\bar{1}\}_{B19'}$ twin boundary. The observed clusters can form in three equivalent orientations due to the symmetry of the austenite in (111)-oriented films, which are connected through a macroscopic boundary.

We identify two recurring clusters as building blocks for this microstructure. The V-cluster consists of two HPVs, connected by a mesoscopic twin boundary. The second cluster, called triangle cluster, starts out as a V-cluster, but grows much larger. Both clusters therefore consist of the same HPVs. Our microscopic model is statistically relevant, which we show by (inverse) pole figures. The observed variant orientation is in agreement with PTMC and confirms that HPVs with $\langle 011\rangle_{B19'}$ twin boundaries and $\{942\}_{B2}$ habit planes are dominant.

The variant orientation observed in the local and integral measurements can be explained by the phenomenological theory of martensite (PTMC), which shows that variant compatibility on a microscopic level governs the microstructure across all length scales and confirms the suitability of this theory to describe the martensitic microstructure in NiTi. However, the scale bridging hierarchy clearly reveals the importance of the accessible low energy transformation path, which is not covered by PTMC. As a decisive feature for connecting the microscopic and mesoscopic microstructure, we identify the small incompatible areas of the V-cluster. Moreover, the need for a transformation path explains the conversion of habit planes to incompatible boundaries between HPVs. This illustrates that a static analysis of a final martensitic microstructure is not sufficient – in-situ experiments are needed to understand differences to PTMC. Therefore, measurements of habit plane orientation performed post-mortem in a fully martensitic sample often show large scatter and deviate strongly from theoretical predictions.

Declaration of competing interest

The authors declare that they have no known competing financial interests or personal relationships that could have appeared to influence the work reported in this paper.

Data availability

All data is available at https://rodare.hzdr.de/record/2328, DOI: 10.14278/rodare.2328.

Acknowledgements

The authors thank K. Freiberg for the preparation of the FIB lamella for the TEM measurements, and S. Hahn and S. Kar for helpful discussion. This work was supported by the German Research Foundation DFG under grants FA 453/13, 390918228 and 134573208.

Appendix A. Supplementary data

Supplementary data to this article can be found online at https://doi.org/10.1016/j.mtadv.2023.100441.

References

[1] J. Mohd Jani, M. Leary, A. Subic, M.A. Gibson, A review of shape memory alloy research, applications and opportunities, Mater. Des. 56 (2014) 1078–1113, https://doi.org/10.1016/j.matdes.2013.11.084.
[2] D.J. Hartl, D.C. Lagoudas, Aerospace applications of shape memory alloys, Proc. Inst. Mech. Eng. Part G J. Aerosp. Eng. 221 (2007) 535–552, https://doi.org/10.1243/09544100JAERO211.
[3] Y. Fu, H. Du, W. Huang, S. Zhang, M. Hu, TiNi-based thin films in MEMS applications: a review, Sens. Actuators Phys. 112 (2004) 395–408, https://doi.org/10.1016/j.sna.2004.02.019.
[4] H. Hou, E. Simsek, T. Ma, N.S. Johnson, S. Qian, C. Cissé, D. Stasak, N. Al Hasan, L. Zhou, Y. Hwang, R. Radermacher, V.I. Levitas, M.J. Kramer, M.A. Zaeem, A. P. Stebner, R.T. Ott, J. Cui, I. Takeuchi, Fatigue-resistant high-performance elastocaloric materials made by additive manufacturing, Science 366 (2019) 1116–1121, https://doi.org/10.1126/science.aax7616.
[5] S. Miyazaki, Y.Q. Fu, W.M. Huang (Eds.), Thin Film Shape Memory Alloys - Fundamentals and Device Applications, Cambridge University Press, Cambridge, 2009.
[6] M. Kohl, Shape Memory Microactuators, Springer Berlin Heidelberg, 2013.
[7] H. Ossmer, C. Chluba, S. Kauffmann-Weiss, E. Quandt, M. Kohl, TiNi-based films for elastocaloric microcooling— fatigue life and device performance, Apl. Mater. 4 (2016), 064102, https://doi.org/10.1063/1.4948271.
[8] P. Velvaluri, M.S. Pravdivtseva, P. Berg, F. Wodarg, R.L. de Miranda, J. Hövener, O. Jansen, E. Quandt, Thin-film patient-specific flow diverter stents for the treatment of intracranial aneurysms, Adv. Mater. Technol. 6 (2021), 2100384, https://doi.org/10.1002/admt.202100384.
[9] T. Waitz, D. Spišák, J. Hafner, H.P. Karnthaler, Size-dependent martensitic transformation path causing atomic-scale twinning of nanocrystalline NiTi shape memory alloys, Europhys. Lett. 71 (2005) 98, https://doi.org/10.1209/epl/i2005-10061-y.
[10] K. Madangopal, R. Banerjee, The lattice invariant shear in Ni-Ti shape memory alloy martensites, Scripta Metall. Mater. 27 (1992) 1627–1632, https://doi.org/10.1016/0956-716X(92)90156-9.
[11] L. Hu, S. Jiang, S. Liu, Y. Zhang, Y. Zhao, C. Zhao, Transformation twinning and deformation twinning of NiTi shape memory alloy, Mater. Sci. Eng. 660 (2016) 1, https://doi.org/10.1016/j.msea.2016.02.066.
[12] J.X. Zhang, M. Sato, A. Ishida, Structure of martensite in sputter-deposited Ti–Ni thin films containing Guinier–Preston zones, Acta Mater. 49 (2001) 3001–3010, https://doi.org/10.1016/S1359-6454(01)00204-X.
[13] J.X. Zhang, M. Sato, A. Ishida, Structure of martensite in sputter-deposited Ti-Ni thin films containing homogeneously distributed Ti_2Ni precipitates, Philos. Mag. A 82 (2002) 1433–1449, https://doi.org/10.1080/01418610208235681.
[14] C. Chluba, W. Ge, R.L. de Miranda, J. Strobel, L. Kienle, E. Quandt, M. Wuttig, Ultralow-fatigue shape memory alloy films, Science 348 (2015) 1004–1007, https://doi.org/10.1126/science.1261164.
[15] S. Miyazaki, K. Otsuka, C.M. Wayman, The shape memory mechanism associated with the martensitic transformation in Ti-Ni alloys - I. self-accommodation, Acta Metall. 37 (1989) 1873–1884.
[16] M. Nishida, T. Nishiura, H. Kawano, T. Inamura, Self-accommodation of B19' martensite in Ti–Ni shape memory alloys – Part I. Morphological and crystallographic studies of the variant selection rule, Philos. Mag. A 92 (2012) 2215–2233, https://doi.org/10.1080/14786435.2012.669858.
[17] K. Madangopal, The self accommodating martensitic microstructure of NiTi shape memory alloys, Acta Mater. 45 (1997) 5347–5365, https://doi.org/10.1016/S1359-6454(97)00161-4.
[18] O. Molnárová, P. Šittner, J. Veselý, M. Cieslar, TEM analysis of deformation bands created by tensile deformation of superelastic NiTi wires, Mater. Char. 167 (2020), 110470, https://doi.org/10.1016/j.matchar.2020.110470.
[19] C. Cayron, What EBSD and TKD tell us about the crystallography of the martensitic B2-B19' transformation in NiTi shape memory alloys, Crystals 10 (2020) 562, https://doi.org/10.3390/cryst10070562.
[20] X. Bian, L. Heller, L. Kadeřávek, P. Šittner, In-situ synchrotron X-ray diffraction texture analysis of tensile deformation of nanocrystalline NiTi wire in martensite state, Appl. Mater. Today 26 (2022), 101378, https://doi.org/10.1016/j.apmt.2022.101378.
[21] A.N. Bucsek, D.C. Pagan, L. Casalena, Y. Chumlyakov, M.J. Mills, A.P. Stebner, Ferroelastic twin reorientation mechanisms in shape memory alloys elucidated with 3D X-ray microscopy, J. Mech. Phys. Solid. 124 (2019) 897–928, https://doi.org/10.1016/j.jmps.2018.12.003.
[22] S. Kauffmann-Weiss, S. Hahn, C. Weigelt, L. Schultz, M.F.-X. Wagner, S. Fähler, Growth, microstructure and thermal transformation behaviour of epitaxial Ni-Ti films, Acta Matererialia 132 (2017) 255–263, https://doi.org/10.1016/j.actamat.2017.04.049.
[23] J. Buschbeck, J. Kawasaki, T.E. Buehl, A.C. Gossard, C.J. Palmstøm, Growth of epitaxial NiTi shape memory alloy films on GaAs(001) and evidence of martensitic transformation, J. Vac. Sci. Technol. B 29 (2011), 03C116, https://doi.org/10.1116/1.3556973.
[24] J. Buschbeck, J.K. Kawasaki, A. Kozhanov, R.D. James, C.J. Palmstrøm, Martensite transformation of epitaxial Ni-Ti films, Appl. Phys. Lett. 98 (2011), 191901, https://doi.org/10.1063/1.3589361.
[25] R.M.S. Martins, N. Schell, M. Beckers, R.J.C. Silva, K.K. Mahesh, F.M.B. Fernandes, Role of the substrate on the growth of Ni-Ti sputtered thin films, Mater. Sci. Eng. 481–482 (2008) 626–629, https://doi.org/10.1016/j.msea.2006.12.225.
[26] S. Schwabe, R. Niemann, A. Backen, D. Wolf, C. Damm, T. Walter, H. Seiner, O. Heczko, K. Nielsch, S. Fähler, Building hierarchical martensite, Adv. Funct. Mater. 31 (2021), 2005715, https://doi.org/10.1002/adfm.202005715.
[27] K. Bhattacharya, Self-accommodation in martensite, Arch. Ration. Mech. Anal. 120 (1992) 201–244, https://doi.org/10.1007/BF00375026.
[28] W.-N. Hsu, E. Polatidis, M. Šmíd, N. Casati, S. Van Petegem, H. Van Swygenhoven, Load path change on superelastic NiTi alloys: in situ synchrotron XRD and SEM DIC, Acta Mater. 144 (2018) 874–883, https://doi.org/10.1016/j.actamat.2017.11.035.
[29] T. Waitz, V. Kazykhanov, H.P. Karnthaler, Martensitic phase transformations in nanocrystalline NiTi studied by TEM, Acta Mater. 52 (2004) 137–147, https://doi.org/10.1016/j.actamat.2003.08.036.
[30] K. Otsuka, X. Ren, Physical metallurgy of Ti–Ni-based shape memory alloys, Prog. Mater. Sci. 50 (2005) 511–678, https://doi.org/10.1016/j.pmatsci.2004.10.001.
[31] M.S. Wechsler, D.S. Lieberman, T.A. Read, On the theory of the formation of martensite, Trans. Am. Inst. Min. Metall. Eng. 197 (1953) 1503.
[32] J.S. Bowles, J.K. Mackenzie, The crystallography of martensite transformations, Acta Metall. 2 (1954) 129–137, https://doi.org/10.1016/0001-6160(54)90102-9.
[33] K. Bhattacharya, Microstructure of Martensite: Why it Forms and How it Gives Rise to the Shape-Memory Effect, Oxford University Press, Oxford, 2003.
[34] M. Nishida, H. Ohgi, I. Itai, A. Chiba, K. Yamauchi, Electron microscopy studies of twin morphologies in B19' martensite in the Ti-Ni shape memory alloy, Acta Metall. Mater. 43 (1995) 1219–1227, https://doi.org/10.1016/0956-7151(94)00332-C.
[35] T. Onda, Y. Bando, T. Ohba, K. Otsuka, Electron microscopy study of twins in martensite in a Ti-50.0 at% Ni alloy, Mater. Trans., JIM 33 (1992) 354–359.
[36] K.M. Knowles, D.A. Smith, The crystallography of the martensitic transformation in equiatomic nickel-titanium, Acta Metall. 29 (1981) 101–110, https://doi.org/10.1016/0001-6160(81)90091-2.
[37] S.P. Gupta, A.A. Johnson, Morphology and crystallography of β' martensite in TiNi alloys, Trans. Jpn. Inst. Met. 14 (1973) 292–302.
[38] K.M. Knowles, A high-resolution electron microscope study of nickel-titanium martensite, Philos. Mag. A 45 (1982) 357–370, https://doi.org/10.1080/01418618208236176.
[39] K. Madangopal, The self accommodating martensitic microstructure of NiTi shape memory alloys, Acta Mater. 45 (1997) 5347–5365, https://doi.org/10.1016/S1359-6454(97)00161-4.
[40] M. Nishida, E. Okunishi, T. Nishiura, H. Kawano, T. Inamura, S. Ii, T. Hara, Self-accommodation of B19' martensite in Ti–Ni shape memory alloys – Part II. Characteristic interface structures between habit plane variants, Philos. Mag. A 92 (2012) 2234–2246, https://doi.org/10.1080/14786435.2012.669860.
[41] T. Inamura, T. Nishiura, H. Kawano, H. Hosoda, M. Nishida, Self-accommodation of B19' martensite in Ti–Ni shape memory alloys. Part III. Analysis of habit plane variant clusters by the geometrically nonlinear theory, Philos. Mag. A 92 (2012) 2247–2263, https://doi.org/10.1080/14786435.2012.669859.
[42] K. Lünser, A. Undisz, K. Nielsch, S. Fähler, How to grow single-crystalline and epitaxial NiTi films in (100)- and (111)-orientation, J. Phys. Mater. 6 (2023), 035002, https://doi.org/10.1088/2515-7639/acd604.
[43] J.D. Sugar, A.W. Cummings, B.W. Jacobs, D.B. Robinson, A free matlab script for spatial drift correction, Microsc. Today. 22 (2014) 40–47, https://doi.org/10.1017/S1551929514000790.
[44] R. Hielscher, H. Schaeben, A novel pole figure inversion method: specification of the MTEX algorithm, J. Appl. Crystallogr. 41 (2008) 1024–1037, https://doi.org/10.1107/S0021889808030112.
[45] F. Bachmann, R. Hielscher, H. Schaeben, Texture analysis with MTEX – free and open source software toolbox, Solid State Phenom. 160 (2010) 63–68. https://dx.doi.org/10.4028/www.scientific.net/SSP.160.63.
[46] K. Lünser, A. Undisz, M.F.-X. Wagner, K. Nielsch, S. Fähler, Data Publication: Solving the Puzzle of Hierarchical Martensitic Microstructures in NiTi by (111)-oriented Epitaxial Films [Data Set], 2023, https://doi.org/10.14278/rodare.2328.
[47] G.M. Michal, R. Sinclair, The structure of TiNi martensite, Acta Crystallogr. B 37 (1981) 1803–1807, https://doi.org/10.1107/S0567740881007292.
[4][8]] R. Niemann, A. Backen, S. Kauffmann-Weiss, C. Behler, , U.\ Rößler K, H. Seiner, O. Heczko, K. Nielsch, L. Schultz, S. Fähler, Nucleation and growth of hierarchical martensite in epitaxial shape memory films, Acta Mater. 132 (2017) 327, https://doi.org/10.1016/j.actamat.2017.04.032.
[49] K.F. Hane, T.W. Shield, Microstructure in the cubic to monoclinic transition in titanium–nickel shape memory alloys, Acta Mater. 47 (1999) 2603–2617, https://doi.org/10.1016/S1359-6454(99)00143-3.
[50] T. Inamura, T. Nishiura, H. Kawano, H. Hosoda, M. Nishida, Self-accommodation of B19' martensite in Ti–Ni shape memory alloys. Part III. Analysis of habit plane

variant clusters by the geometrically nonlinear theory, Philos. Mag. A 92 (2012) 2247–2263, https://doi.org/10.1080/14786435.2012.669859.
[51] T. Teramoto, K. Nagahira, K. Tanaka, Geometry and energy barrier of martensite in the initial stage martensitic transformation in B19' TiNi shape memory alloy, Acta Mater. 201 (2020) 94–101.
[52] G. Laplanche, J. Pfetzing-Micklich, G. Eggeler, Orientation dependence of stress-induced martensite formation during nanoindentation in NiTi shape memory alloys, Acta Mater. 68 (2014) 19–31, https://doi.org/10.1016/j.actamat.2014.01.006.
[53] M.F.-X. Wagner, S. Pfeiffer, Prediction of NiTi B19' martensite twin activation below a spherical indenter tip, Shape Mem. Superelasticity. 5 (2019) 313–326, https://doi.org/10.1007/s40830-019-00238-1.
[54] J. Pfetzing-Micklich, M.F.-X. Wagner, R. Zarnetta, J. Frenzel, G. Eggeler, A. E. Markaki, J. Wheeler, T.W. Clyne, Nanoindentation of a pseudoelastic NiTiFe shape memory alloy, Adv. Eng. Mater. 12 (2010) 13–19, https://doi.org/10.1002/adem.200900266.
[55] S. Kaufmann, R. Niemann, T. Thersleff, U.K. Rößler, O. Heczko, J. Buschbeck, B. Holzapfel, L. Schultz, S. Fähler, Modulated martensite: why it forms and why it deforms easily, New J. Phys. 13 (2011), 053029, https://doi.org/10.1088/1367-2630/13/5/053029.
[56] E. Hornbogen, Fractal dimensions of martensitic microstructures, ESOMAT 1989 - ist, Eur. Symp. Martensitic Transform. Sci. Technol. (1989) 97–104, https://doi.org/10.1051/esomat/198902008.
[57] S. Matthies, On the reproducibility of the orientation distribution function of texture samples from pole figures (Ghost phenomena), Phys. Status Solidi B 92 (1979), https://doi.org/10.1002/pssb.2220920254. K135–K138.
[58] H.J. Bunge, P.R. Morris, C.U. Nauer-Gerhardt, ODF-analysis of multipeak textures, Textures Microstruct. 11 (1989) 1–22, https://doi.org/10.1155/TSM.11.1.
[59] S. Miyazaki, S. Kimura, K. Otsuka, Y. Suzuki, The habit plane and transformation strains associated with the martensitic transformation in Ti-Ni single crystals, Scripta Metall. 18 (1984) 883–888.
[60] O. Matsumoto, S. Miyazaki, K. Otsuka, H. Tamura, Crystallography of martensitic transformation in Ti-Ni single crystals, Acta Metall. 35 (1987) 2137–2144.
[61] T. Saburi, M. Yoshida, S. Nenno, Deformation behavior of shape memory Ti-Ni alloy crystals, Scripta Metall. 18 (1984) 363–366, https://doi.org/10.1016/0036-9748(84)90453-8.
[62] A.N. Bucsek, L. Casalena, D.C. Pagan, P.P. Paul, Y. Chumlyakov, M.J. Mills, A. P. Stebner, Three-dimensional in situ characterization of phase transformation induced austenite grain refinement in nickel-titanium, Scripta Mater. 162 (2019) 361–366, https://doi.org/10.1016/j.scriptamat.2018.11.043.
[63] T. Waitz, The self-accommodated morphology of martensite in nanocrystalline NiTi shape memory alloys, Acta Mater. 53 (2005) 2273–2283, https://doi.org/10.1016/j.actamat.2005.01.033.
[64] W. Huang, Effects of internal stress and martensite variants on phase transformation of NiTi shape memory alloy, J. Mater. Sci. Lett. 17 (1998) 1843–1844, https://doi.org/10.1023/A:1006682226289.
[65] H.M. Paranjape, P.P. Paul, B. Amin-Ahmadi, H. Sharma, D. Dale, J.Y.P. Ko, Y. I. Chumlyakov, L.C. Brinson, A.P. Stebner, In situ, 3D characterization of the deformation mechanics of a superelastic NiTi shape memory alloy single crystal under multiscale constraint, Acta Mater. 144 (2018) 748–757, https://doi.org/10.1016/j.actamat.2017.11.026.
[66] X. Bian, L. Heller, O. Tyc, L. Kadeřávek, P. Šittner, In-situ synchrotron x-ray diffraction texture analysis of tensile deformation of nanocrystalline superelastic NiTi wire at various temperatures, Mater. Sci. Eng. 853 (2022), 143725, https://doi.org/10.1016/j.msea.2022.143725.
[67] M. Thomas, O. Heczko, J. Buschbeck, L. Schultz, S. Fähler, Stress induced martensite in epitaxial Ni–Mn–Ga films deposited on MgO(001), Appl. Phys. Lett. 92 (2008), 192515, https://doi.org/10.1063/1.2931082.